Title
Compromised Integrity of Central Visual Pathways in Patients With Macular DegenerationCompromised Integrity of Central Visual Pathways in MD

Journal
Investigative Ophthalmology & Visual Science, 58(7)

ISSN
0146-0404

Authors
Malania, Maka
Konrad, Julia
Jägle, Herbert
et al.

Publication Date
2017-06-09

DOI
10.1167/iovs.16-21191

Compromised Integrity of Central Visual Pathways in Patients With Macular Degeneration

Maka Malania,[1] Julia Konrad,[2] Herbert Jägle,[2] John S. Werner,[1,3] and Mark W. Greenlee[1]

[1]Institute for Experimental Psychology, University of Regensburg, Regensburg, Germany
[2]University Eye Hospital, University of Regensburg, Regensburg, Germany
[3]Department of Ophthalmology & Vision Science, University of California, Davis, California, United States

Correspondence: Mark W. Greenlee, Institute for Experimental Psychology, University of Regensburg, Universitaetsstrasse 31, 93053 Regensburg, Germany; mark.greenlee@psychologie.uni-regensburg.de.

Submitted: November 28, 2016
Accepted: May 5, 2017

Citation: Malania M, Konrad J, Jägle H, Werner JS, Greenlee MW. Compromised integrity of central visual pathways in patients with macular degeneration. *Invest Ophthalmol Vis Sci*. 2017;58:2939–2947. DOI:10.1167/iovs.16-21191

Purpose. Macular degeneration (MD) affects the central retina and leads to gradual loss of foveal vision. Although, photoreceptors are primarily affected in MD, the retinal nerve fiber layer (RNFL) and central visual pathways may also be altered subsequent to photoreceptor degeneration. Here we investigate whether retinal damage caused by MD alters microstructural properties of visual pathways using diffusion-weighted magnetic resonance imaging.

Methods. Six MD patients and six healthy control subjects participated in the study. Retinal images were obtained by spectral-domain optical coherence tomography (SD-OCT). Diffusion tensor images (DTI) and high-resolution T1-weighted structural images were collected for each subject. We used diffusion-based tensor modeling and probabilistic fiber tractography to identify the optic tract (OT) and optic radiations (OR), as well as nonvisual pathways (corticospinal tract and anterior fibers of corpus callosum). Fractional anisotropy (FA) and axial and radial diffusivity values (AD, RD) were calculated along the nonvisual and visual pathways.

Results. Measurement of RNFL thickness reveals that the temporal circumpapillary retinal nerve fiber layer was significantly thinner in eyes with macular degeneration than normal. While we did not find significant differences in diffusion properties in nonvisual pathways, patients showed significant changes in diffusion scalars (FA, RD, and AD) both in OT and OR.

Conclusions. The results indicate that the RNFL and the white matter of the visual pathways are significantly altered in MD patients. Damage to the photoreceptors in MD leads to atrophy of the ganglion cell axons and to corresponding changes in microstructural properties of central visual pathways.

Keywords: diffusion tensor imaging, white matter tracts, age-related macular degeneration, juvenile macular dystrophy

---

Macular degeneration (MD) is the end state of several complex diseases linked both to genetic and environmental factors.[1–7] Macular degeneration gradually destroys high spatial and chromatic central vision needed for control of gaze and tasks of everyday life such as reading and driving. The condition currently affects several million people and the prevalence is expected to increase over the coming decades. Patients with MD suffer from scotoma of central vision, and consequently, loss of afferent input to visual cortex. Macular degeneration includes retinal dystrophies such as juvenile macular degeneration (Stargardt disease) and cone-rod dystrophy, as well as AMD. The typical onset of juvenile (hereditary form) retinal dystrophies occurs before age 30 years, while AMD has a much later onset, typically after age 60 years. Like other retinal dystrophies, AMD is heterogeneous in its genetics and morphology. It is first diagnosed by the presence of drusen (extracellular deposits) greater than 63 μm[8] that accumulate between the RPE and Bruch's membrane and consequently disrupt the chorioretinal complex (photoreceptors, retinal pigment epithelium, choriocapillaris, and choroid).

While all major forms of MD lead to outer retinal layer alterations such as photoreceptor and RPE atrophy,[9,10] we hypothesized that inner retinal neurons as well as central visual pathways may also be affected subsequent to photoreceptor degeneration. Early studies in rat models of degeneration found histochemical changes not only in the inner plexiform layer but also in the retinal ganglion cell layer.[11,12] However, the data collected from patients are inconsistent. Rimayanti et al.[13] measured the thickness of the ganglion cell complex (GCC) and retinal nerve fiber layer (RNFL) and found only a weak association between AMD and RNFL thickness reduction. Although GCC thickness was significantly decreased, Lee and Yu[14] investigated 76 eyes classified as having dry AMD. They observed a reduction of macular ganglion cell-inner plexiform layer of about 10% as well as small but significant thinning of RNFL in eyes with dry AMD compared to controls (88.69 vs. 93.96 μm; $P < 0.001$). There are reports of RNFL thickness abnormalities in hereditary retinal diseases such as retinitis pigmentosa, cone-rod dystrophy, and Stargardt disease.[15–17]

In patients with MD, large portions of the central visual pathways normally receiving afferent signals from the fovea will be unstimulated. The neuroanatomic consequences of insufficient afferent and efferent stimulation have been reported in many conditions. Significant atrophy of visual pathways and primary and associated visual cortex were found in congenital and early blind adults.[18–20] Studies based on voxel-based morphometry (VBM) detected gray matter changes in patients with amblyopia in the calcarine sulcus.[21–23] Similar results were shown for glaucoma and macular degeneration patients.[24–28] Plank et al.[29] used VBM techniques to investigate structural brain changes in patients with hereditary retinal dystrophies. They detected gray matter differences between patients and controls around the respective lesion projection zone in the calcarine sulcus, suggesting that the lack of functional input leads to gray matter alterations.

Previous results invite the question of whether central morphologic changes are restricted to gray matter or whether MD affects the white matter (optic nerve and optic radiations) as well. Previous reports that used a voxel-based morphometry technique showed volumetric losses of visual white matter pathways in patients with open-angle glaucoma and AMD.[30,31] Ogawa and colleagues[32] also demonstrated compromised integrity of white matter pathways in patients with Leber hereditary optic neuropathy and cone-rod dystrophy using diffusion tensor imaging (DTI). This technique has been used extensively to investigate microstructural properties of white matter tissue by modeling diffusion of water molecules inside the tissue. In an unstructured space, water molecules diffuse freely in a random manner. In myelinated axons, movement of water molecules is restricted by axonal membranes. This affects the diffusion rate of water molecules (diffusion is greater along the length of axons than perpendicular to them).[33,34] Diffusion is typically described as a 3D ellipsoid through a 3×3 matrix.[35,36] The largest (or primary) ellipsoid eigenvector represents diffusion along the length of a fiber tract and is referred to as the AD. The rate of diffusion in the transverse direction that is calculated as the mean of two secondary eigenvectors is called RD. Another diffusion scalar is FA, which quantifies coherence of water diffusion, with 0 indicating low coherence and 1 indicating higher coherence. While FA is highly sensitive to microstructural changes, it is less specific to the type of change. Clinical and pathologic studies have found that AD tends to reflect axonal integrity, whereas RD corresponds more closely to demyelination.[37–41]

Here we investigate whether retinal damage caused by MD might also alter microstructural properties of visual pathways. This question is relevant to clinical management of MD and understanding the pathogenesis of these diseases. We used spectral-domain optical coherency tomography (SD-OCT) to quantify changes in peripapillary RNFL in MD patients (Stargardt disease or AMD) with bilateral geographic atrophy. Analysis of OCT images revealed RNFL thickness differences between patients and control groups. Diffusion-weighted magnetic resonance imaging (MRI) was used to measure diffusivity properties along the optic tract and optic radiation. We observed a significant change in diffusivity properties of white matter in MD, indicating that retinal damage caused by MD may affect the microstructural properties of central visual pathways. Control analyses of nonvisual pathways demonstrated no significant differences between groups.

METHODS

Participants

Data were collected from six patients with macular degeneration (three with Morbus Stargardt disease and three with age-related macular degeneration) and six age-matched control subjects with normal or corrected to normal vision. Patients were recruited from the Department of Ophthalmology, University Eye Hospital of Regensburg. All subjects were free from other ocular or neurologic diseases and had not undergone any previous laser or intravitreal injection treatment. Inclusion criteria required that patients must have geographic atrophy and binocular central scotomas (>10°) in both eyes.

The mean age of MD patients was 59 years and ranged from 50 to 74 years (two males, four females); the control group's mean age was 59 years and ranged from 50 to 73 years (four males and two females).

All participants underwent detailed ophthalmologic examination by experienced ophthalmologists from the University Eye Hospital, University of Regensburg. Screening tests included visual acuity, Humphrey perimetry, fundus imaging, and SD-OCT. The Table summarizes participants' age, visual acuity, refractive error, disease duration, and scotoma size. We acquired MRI images from participants. Normally, ophthalmologic screening and brain imaging were conducted on the same day or few days apart.

The ethics committee of the University of Regensburg approved all procedures that were in accord with the tenets of the Declaration of Helsinki. All participants provided written informed consent and authorization to use their clinical data for research.

SD-OCT – Retinal Nerve Fiber Thickness

The SD-OCT examination was performed after pupil dilation with 0.5% Tropicamide. A spectral-domain OCT (Heidelberg Spectralis HRA+OCT, Heidelberg Engineering, Inc., Heidelberg, Germany) was used to obtain the retinal images. The circumpapillary OCT images were acquired with 15 B-scans in automatic real time (ART) mode (circle diameter 12°). Figure 1 shows OCT images of one healthy eye and one eye with geographic atrophy. The retinal nerve fiber layer (from the inner margin of the internal limiting membrane to the outer margin of the RNFL layer) was automatically segmented using commercial software (Spectralis version 6.3.2.0; Heidelberg Engineering, Heidelberg, Germany). Manual adjustments were used when the automatic retinal layer segmentation failed. Since patients often fixate with their preferred retinal loci, instead of the fovea, an additional adjustment was performed for fovea-to-disc alignment. We then analyzed the RNFL thickness for the average, and for four sectors (nasal, temporal, inferior, and superior). Results of measurements are plotted in Figure 2. For statistical analyses, a generalized estimating equation (GEE) was used to account for the possible correlation between left and right eyes within-subjects. In the GEE model, RNFL measurements were included as a dependent variable and left/right eye as a within-subject variable. Spearman's correlation coefficient was carried out to evaluate possible correlations between RNFL thickness changes and diffusion properties of optic tract and optic radiation. All statistical tests were performed using commercial software (Statistical Package for the Social Sciences [SPSS] version 21; IBM Corp., Armonk, NY, USA).

MRI Acquisition and Processing

We collected all MRI data with a scanner (3T head-only Allegra; Siemens, Erlangen, Germany) using a one-channel whole head coil. One high-resolution T1-weighted structural volume (160 slices covering the whole brain, $1 \times 1 \times 1$ mm^3 voxel size, FOV $= 256 \times 256$ mm^2) was obtained from each subject using an Alzheimer's Disease Neuroimaging Initiative sequence (TR = 2250 ms, TE = 2.6 ms, FA = 90°, adapted from the Alzheimer's Disease Neuroimaging Project: Laboratory for Neuroimaging, UCLA, Los Angeles, CA, USA).

Diffusion-weighted scans (single-shot pulsed gradient spin-echo sequence with echo planar readout, TR = 7200 ms, TE = 95, FA = 90°) were collected for each subject in two separate

Table. Demographics of Patients (P01–P06) and Controls (C01–C06)

Subject	Sex	Age	Diagnosis	Disease Duration, y	Visual Acuity OD, logMAR	Visual Acuity OS, logMAR	Refractive Error, OD	Refractive Error, OS	Atrophy Size-OD, mm^2	Atrophy Size-OS, mm^2
P01	M	67	AMD	12	1.17	0.65	−4.0 + 0.25 × 110	−4.25 + 0.75 × 19	43.32	45.45
P02	F	66	AMD	9	0.93	0.93	−2.25 + 1.0 × 80	−3.5 + 0.5 × 24	32.6	28.04
P03	F	74	AMD	14	1.37	1.37	+2.0 + 1.5 × 165	+2.25 + 2.75 × 135	18.49	19.47
P04	F	49	Stargardt	34	0.93	0.89	0	−0.5 + 0.25 × 150	6.37	3.6
P05	F	50	Stargardt	16	−1.22	−1.24	+1.25 + 0.5 × 5	+2.0 + 0.75 × 162	9.49	9.39
P06	M	49	Stargardt	29	0.89	0.89	−0.5 + 0.5 × 5	−0.5 + 1.0 × 2	15.3	12.27
C01	M	51	-	-	−0.02	−0.02	+0.25 + 0.25 × 0	+0.75 + 0.5 × 0	-	-
C02	M	64	-	-	−0.03	−0.05	−1.25 + 0.25 × 173	−0.25 + 0.5 × 90	-	-
C03	F	50	-	-	0.1	−0.02	−0.75 + 0.5 × 75	+0,5 + 0.5 × 130	-	-
C04	M	48	-	-	0.1	−0.11	−5.0 + 0.5 × 60	−6.5 + 0.5 × 150	-	-
C05	M	73	-	-	0.27	0.26	+1.25 + 0.5 × 81	+1.0 + 0.5 × 59	-	-
C06	F	65	-	-	0.21	0.21	+3.0 + 3.75 × 75	−1.5 + 1.0 × 90	-	-

According to sex, age, diagnosis, duration of disease, visual acuities, refractive error, and atrophy sizes for right and left eyes (diameter in mm^2).

sessions. The diffusion weighting orientations were isotropically distributed along 35 directions by using a b-value of 1000 s/mm^2. Five volumes without diffusion weighting (b-value of zero) were interleaved into the diffusion sequence after every six volumes. The 54 sagittal slices covered the whole brain (voxel size = 2.5 × 2.5 × 2.5 mm^3).

Anatomic images were aligned to the anterior commissure-posterior commissure (AC-PC) plane using a VistaLab software package for anatomic data preprocessing (software is freely available from https://github.com/vistalab/vistasoft/). In order to make AC-PC alignment, we manually defined localization of AC, PC, and midsagittal planes. Then, anatomic images were further processed for cortical reconstruction and segmentation using FreeSurfer version 5.1.0 (Martinos Center for Biomedical Imaging, Charlestown, MA, USA) as described elsewhere.[42] Finally, automatic parcellation of the cerebral cortex was performed based on gyral and sulcal structure.[43,44]

Diffusion-weighted image preprocessing and fiber tracking was conducted with VistaLab software in a computing environment (MATLAB 2012b; MathWorks, Inc., Natick, MA, USA). All nondiffusion ($b = 0$) images were first averaged and motion corrected. Then, Eddy current and motion corrections (six parameters, rigid-body registration) were applied to the diffusion-weighted images and registered to the mean non-diffusion-weighted images using a rigid body mutual information algorithm.[45,46] The rotation component of the omnibus coordinate transform has been applied to the diffusion-weighting gradient directions to preserve their orientation with respect to the resampled diffusion images. Finally, the corrected diffusion-weighted image was aligned to AC-PC in the T1-weighted image. In order to create FA, AD, and RD maps, tensors were fit using the 'least-square' tensor estimation (bootstrapped 500 times per voxel[35]).

ROI Identification

The pericalcarine cortex of the left and right hemispheres and optic chiasm were extracted from the FreeSurfer parcellation file. A 4-mm radius sphere was placed on the location of the optic chiasm that was further used as the starting point ROI for the optic tract. Coordinates of the lateral geniculate nuclei (LGN) were estimated with help of an LGN atlas computed as average MNI coordinates across 30 subjects. Then we placed a 4.5-mm radius spherical ROI at the LGN location. The size of the LGN ROI (360 mm^3) was chosen to include the entire LGN.

Fiber Tracking

Probabilistic fiber tracking was performed with ConTrack[47] to identify optic tract (OT) and optic radiations (OR). The ConTrack differs from other probabilistic fiber tracking methods in the way that it combines two steps: first, pathway sampling and second, pathway scoring. During pathway sampling, ConTrack performs pathway sampling by generating a large set of potential pathways, while pathway scoring involves computing a confidence value for each pathway sample based on its anatomic validity. ConTrack is a valid and reliable procedure for visual pathway tracking that is confirmed by multiple studies.[32,48–50] To generate OT, we sampled 5000 candidate pathways between the optic chiasm and LGN and kept the 100 most likely fibers applying the ConTrack scoring algorithm. We repeated this procedure both for left and right hemispheres. To identify OR, 100,000 candidate fibers were sampled between the LGN and calcarine sulcus. After applying the scoring algorithm about 30% of these fibers were retained. Once initial pathway estimates were created, we manually removed any fiber that took nonbiologic paths (e.g., crossing from one to the other hemisphere or passing through CSF). Figure 3 shows an axial view of the optic tract and optic radiation in one control subject.

We identified the core of each fiber tract by applying an algorithm implemented in the automatic fiber quantification (AFQ) software package.[51] Each tract was partitioned into 100 equally sized parts creating 100 segments. Diffusivity properties were calculated at each segment using spline interpolation of the diffusivity properties. To obtain a summary of the tract profile, diffusivity measurements of both left and right tracts were combined and only 80 central segments were analyzed. The first and the last 10 segments out of 100 were excluded in order to avoid partial-volume effects. In addition, the optic radiations were divided into five groups according to their mean fiber length (based on percentile). We also reconstructed corticospinal tract and anterior forceps of corpus callosum as control fiber tracks because they would not be expected to differ for our two groups (Fig. 4). We used the AFQ[51] toolbox that automatically creates tract profiles for 18 major white matter tracts, including corticospinal tract and corpus callosum.

The significance of the difference in the diffusion parameters between MD patients and controls was determined using Wilcoxon's rank-sum test. In addition, we performed segment-by-segment analyses to determine the approximate location of

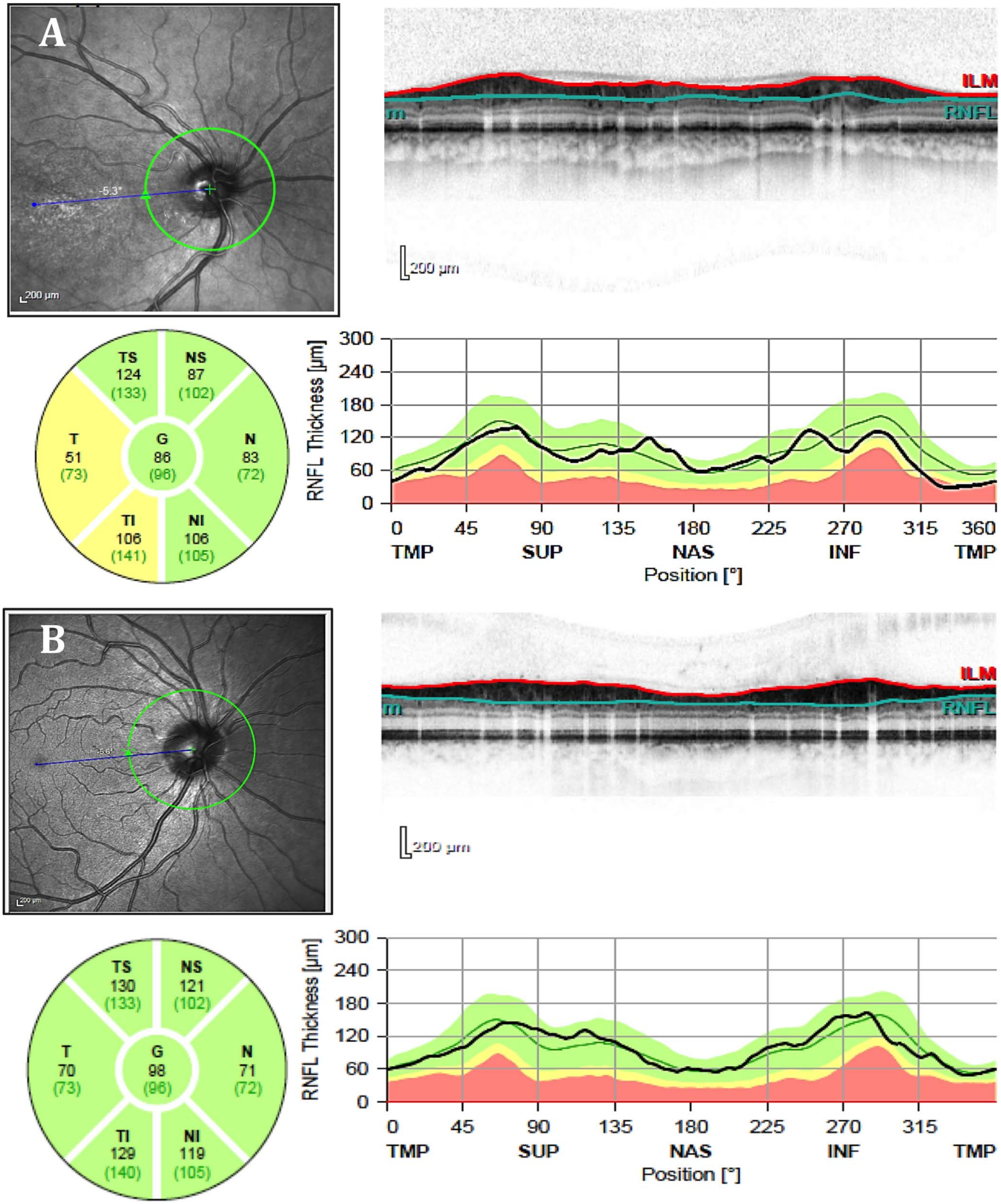

FIGURE 1. Images of SD-OCT acquired with an HRA+OCT device (Heidelberg Engineering) for two participants. (**A**) Patient with geographic atrophy due to MD (age = 50 years). (**B**) Normal eye (51 years). Fundus images are shown with a circle denoting the position of the circumpapillary scan. The right carts display the cross-section of circumpapillary area of retina (*Red contour* indicates internal limiting membrane; *green* outlines inner border of RNFL). Circular profiles below the fundus images show RNFL thickness (µm) at the different retinal locations (nasal-superior [NS]; nasal [N]; nasal-inferior [NI]; temporal-inferior [TI]; temporal [T]; and temporal-superior [TS]) and as an average of the total ring scan (G). The plots to the right show the RNFL profiles.

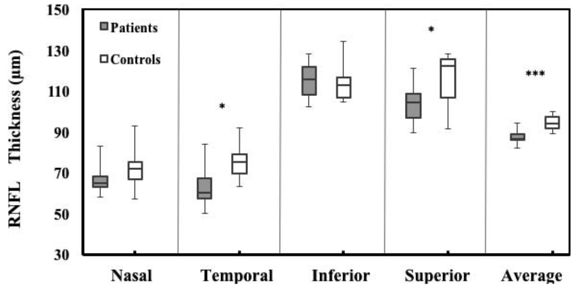

Figure 2. Circumpapillary RNFL thickness measured (patients $n = 5$; controls $n = 6$) by SD-OCT as illustrated in Figure 1 and plotted for the nasal, temporal, inferior, and superior segments, as well as average RNFL thickness is reported. Data are presented as a Tukey *box-and-whiskers* plot and an * denotes statistically significant differences between MD patients and controls.

abnormalities using 1-way ANOVAs. The results of segment-by-segment analyses are shown as light bluish-gray bars superimposed on the tract profile curves. The statistical analyses were performed using a statistical toolbox package (MATLAB 2015a; MathWorks, Inc.).

RESULTS

Optical Coherence Tomography

Compared to healthy controls, patients with MD had significant thinning of RNFL thickness at the temporal (reduced by 16%, $P = 0.019$) and superior segments (reduced by 11%, $P = 0.018$) of the circumpapillary area of retina. Thickness of RNFL was also reduced in the nasal segment by 7%, although no significant difference between groups was found ($P = 0.21$). Comparison of average RNFL thickness reveals a significant loss in MD patients ($P < 0.0001$). Measurements of OCT of one patient are excluded from statistical analyses because of poor segmentation due to spread of the geographic atrophy extending toward the optic nerve head. On OCT images, the margins between retinal layers were washed out and it was not possible to produce a reliable segmentation. Results of the OCT measurements are presented in Figure 2.

Tract Profile

Fractional anisotropy (FA), and axial and radial diffusivity values (AD, RD) were calculated along the OT and OR. We identified visual tract profiles in six patients (12 hemispheres) and six healthy control subjects (12 hemispheres).

Tract profiles of OT and OR were compared between patients and healthy controls. Figure 5 shows mean differences of FA values averaged across hemispheres. We found a significant decrease in FA values in MD patients both in OT ($P < 0.005$) and OR ($P < 0.000001$) compared to the age-matched control group. An upper and lower panel of Figure 6 compares group means of AD and RD values, respectively. Axial diffusivity values significantly changed in optic radiation ($P < 0.0005$); however, no changes in AD were observed in optic tract of patients ($P > 0.05$). In contrast, RD is significantly elevated in optic tracts ($P < 0.0005$) of patients while no significant increase of RD was found in optic radiation ($P > 0.05$) compared to controls.

Analyses of corticospinal tract and anterior fibers of corpus callosum did not reveal any statistically significant differences of FA values between patients and controls ($P = 0.19$ and $P = 0.35$, respectively).

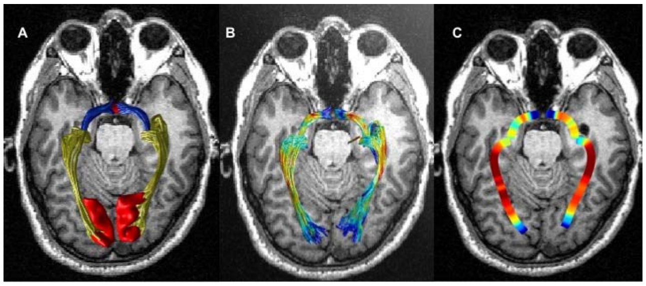

Figure 3. Visual pathways. (**A**) Demonstrates reconstruction of OT (*blue*) and OR (*yellow*) using ConTrack fiber tractography method in a representative subject. Fibers are superimposed on the axial slice of the T1-weighted image. Regions of interest (optic chiasm and calcarine sulcus) are shown in *red*. (**B**) Rendered OT and OR. Heat maps correspond to FA values in voxels (*red,* high FA; *blue*, low FA). (**C**) Averaged FA values along the OR and OT based on linear sum of individual voxel FA value weighted by its distance from the core of the pathway.

Results of Spearman's correlation test revealed a significant correlation between FA values and RNFL thickness in the optic nerve for patients ($r = 0.703$, $P = 0.023$) while the correlation for optic radiation is not significant ($r = 4.33$. $P = 0.211$). However, no correlation was observed between RFNL thickness and FA values neither in optic tract ($r = 0.4$, $P = 0.18$) nor in optic radiation ($r = 0.38$, $P = 0.22$) in control subjects.

In addition, we analyzed FA values in OR fibers that are grouped into five categories based on fiber length (by percentile). The shortest group is thought to be retinal projections from the lower peripheral visual field; the longest groups process information from the upper peripheral visual field; the three middle groups carry foveal signals. Results are plotted in Figure 7. Values of FA were significantly lower in all five fiber groups, although the losses due to MD are greater in the short and middle fiber groups (fiber groups 0–20, $P < 0.0000001$; fiber groups 20–40, $P < 0.00000001$; fiber groups 40–60, $P < 0.00000001$; fiber groups 60–80, $P < 0.000001$; fiber groups 80–100, $P < 0.005$).

DISCUSSION

Visual information transmission requires a highly organized set of processes involving the entire visual system, starting at the retina, continuing through the visual pathways, and in the topographic maps of visual cortex. Damage at any stage of the visual system may disturb the functioning of other stages. In the current study, it was assumed that MD, which causes degeneration of the outer retina and photoreceptor dysfunction, could affect inner retinal neurons and could provoke microstructural changes in the nerve fibers of central visual pathways. To test our hypotheses, optic tract and optic radiations were reconstructed and analyzed along with two additional nonvisual pathways (corticospinal tract and anterior fibers of corpus callosum). There is agreement that the corticospinal tract participates in control of motor functions while anterior fibers of the corpus callosum that connects left and right frontal lobes participates in such high level functions as decision making. Data analyses demonstrate that diffusivity properties of nonvisual pathways are not affected by MD. However, we found significant diffusion abnormalities along the visual pathways in MD patients.

Here we have shown, in agreement with previous studies,[11–17] that damage of the photoreceptor layer affects more inner retinal layers such as RNFL and ultimately impacts the integrity of central visual pathways. Morphologic studies

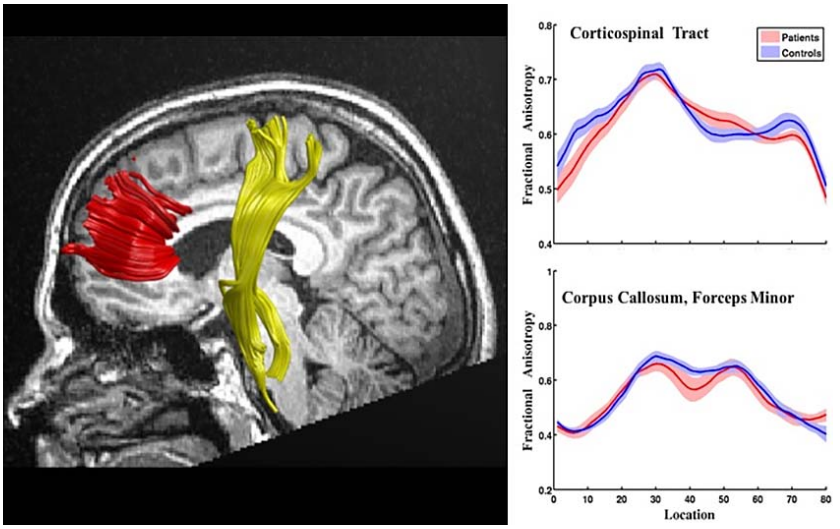

Figure 4. The left chart displays reconstruction of corticospinal tract (*yellow*) and anterior forceps of corpus callosum (*red*) in a representative subject. Fibers are superimposed on the sagittal slice of the T1-weighted image. The *right panel* shows FA values plotted along corticospinal tract and anterior forceps of corpus callosum. The thick curves show mean of each group (*red*, averaged over 6 patients; *blue*, averaged over 6 controls); the light shaded areas represent ± 1 SEM. We found no significant differences between groups in the nonvisual pathways.

that investigated the retinal nerve fiber bundle trajectories demonstrated that foveal fibers occupy a large portion of the temporal part of the optic nerve head.[52,53] If so, we would expect to find changes in the temporal part of retina of MD patients. Indeed, comparing RNFL thickness in normal eyes to that with MD, we found a 16% reduction of RNFL thickness in patients at the temporal segment of retina. The conflicting reports regarding RNFL thinning in eyes with MD may be explained by the diversity of methods used as well as by differences in study patients (i.e., in the pathogenesis of MD, multiple genes and environmental factors play a role). In addition, duration and severity of disease are likely to have an effect on the degree of change in the inner layers of the retina. The mechanisms underlying these changes currently remain unclear. We can only speculate that one of the reasons might be transsynaptic degeneration.[16]

The question is: What may have caused the diffusivity parameter alteration in visual white matter pathways of MD patients? It has been suggested that reduced oligodendroglial integrity or changes in the axonal diameters or density is associated with an increase in radial diffusivity, whereas primary injury to axons, such as Wallerian degeneration, is associated with a decrease in axial diffusivity.[37,38,54,55] Fractional anisotropy is highly sensitive to microstructural changes but less specific to the type of change. It is a normalized measure of the fraction of the tensor's magnitude (i.e., FA is significantly modulated by the ratio between radial and axial diffusivity). Thus, by analyzing FA with RD and AD, it is possible to distinguish between diffusivity patterns with different neurobiologic foundations. In the optic tract, we found significantly increased RD in the patient group while there was only a small difference in AD values between groups. On the other hand, AD is reduced significantly along the optic radiation in patients while RD remains more or less intact. Pathologic substrates that underlie such alternations in diffusivity are yet to be fully clarified. A difference in characteristics of diffusion abnormalities between optic tract and optic radiation was also reported by Ogawa et al.[32] in other ocular diseases. One can only speculate that transneuronal

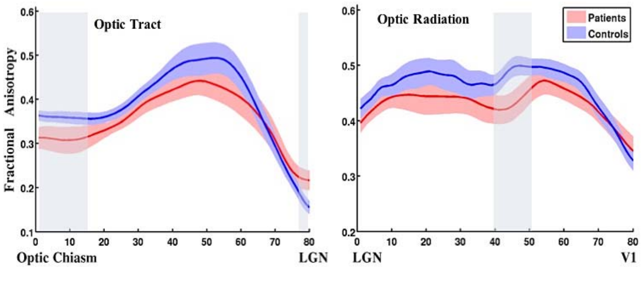

Figure 5. Fractional anisotropy values along the core of the optic tract and optic radiation. *Bold* contours correspond to the mean of each group (*red,* patients; *blue*, control group). Analyses were performed on groups of six MD patients and six control subjects. The *light shaded* areas show ± 1 SEM. *Shaded grayish-blue* bars indicate the portion of the tract showing a significant main effect of subject groups (1-way ANOVA, $P < 0.05$).

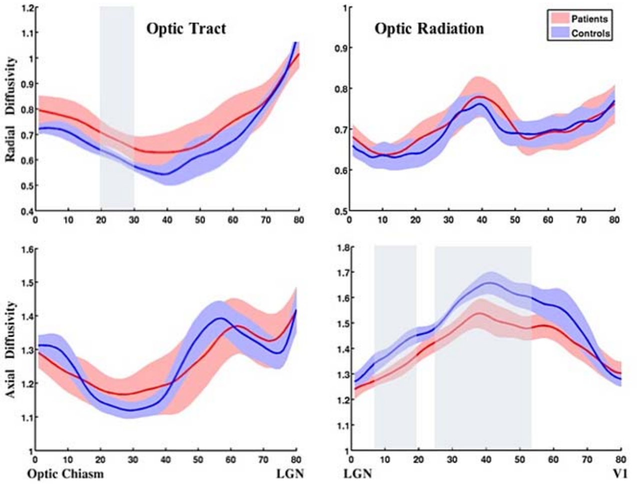

Figure 6. Hemisphere-averaged group tract profiles showing axial and radial diffusivity along the core of the optic tract and optic radiation. Bold contours correspond to the mean of each group (patients, $n = 6$; controls, $n = 6$); The *light shaded* areas show ± 1 SEM. *Shaded grayish-blue bars* indicate the portion of the tract showing a significant main effect of subject groups (1-way ANOVA, $P < 0.05$).

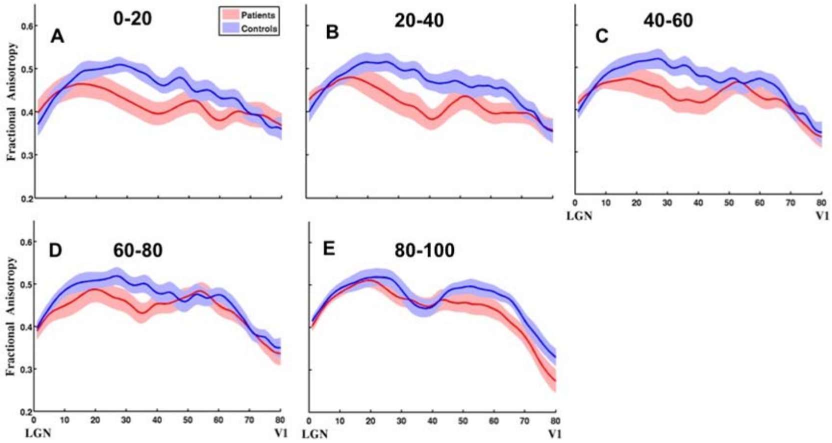

FIGURE 7. Fractional anisotropy along optic radiation fiber groups divided by length. Optic radiation fibers are grouped into five categories based on fiber length by percentile from short to long. (**A**) 0–20. (**B**) 20–40. (**C**) 40–60. (**D**) 60–80. (**E**) 80–100. Symbols as shown in Figure 5.

degeneration could potentially have a different effect on anterior and posterior parts of visual pathways based on their morphologic properties and anatomical structures.

We also evaluated the relationship between FA values and RNFL thickness changes. Low FA in optic tract was found to be correlated with RNFL thinning. One plausible explanation for these findings is that abnormal FA values in the optic tract may reflect axonal loss or reduction of glial cells in RNFL. However, there was no significant correlation between RNFL and diffusivity changes in optic radiation.

Additional analysis of optic radiations, divided into five groups based on fiber length, was performed. From anatomic studies, three groups of bundles can be distinguished in the optic radiations: (1) the anterior-ventral fiber bundle, also termed Meyer's loop, that carries information from the upper peripheral visual field and contains the longest fiber fascicles; (2) the dorsal bundle, a short direct segment that carries signals from the lower visual field; and (3) the central bundle, the longer direct fibers that transmits foveal signals. Values of FA were extracted from each group of fibers and compared between patients and controls. In patients with MD, we found significantly lower FA values in all five fiber groups, where the short and middle fiber groups, that which correspond to dorsal and central bundles, showed a more pronounced effect. One interpretation could be that when we are dealing with the advanced form of MD not only the segment of fibers receiving input from the fovea is affected, but the peripheral afferent fibers also suffer from malfunction. Our finding of overall RNFL thickness reduction in MD patients is consistent with this suggestion.

CONCLUSIONS

We demonstrated that damage to the photoreceptors in MD leads to atrophy of the ganglion cell axons, as evidenced by thinning of the RNFL in SD-OCT, and to corresponding changes in diffusivity parameters of central visual pathways detected by MRI/DTI. Control measurements of diffusivity parameters in corticospinal and anterior forceps of corpus callosum suggest that these findings are specific to the visual pathways.

We suggest that microstructural changes discovered in central visual white matter pathways in individuals with MD are probably driven by the lack of input to a population of neurons. The assessment of the impact of various eye diseases on the visual pathways is important to obtain a precise diagnosis of the ocular disease in individual patients. In addition, this information might be critical when selecting patients to receive retinal implants, because transmission of signals delivered from such implants requires intact visual white matter pathways. Our findings suggest that future therapies for MD should be initiated as early as possible to avoid long-term and perhaps irreversible damage to visual pathways.

Acknowledgments

The authors thank Horst Helbig, MD, and Eva Kopezky, MD, for their support.

Supported by Deutsche Forschungsgemeinschaft (GR988/18-2, FOR 1075 Regulation and pathology of homeostatic processes in visual function), the Alexander von Humboldt Foundation, and by the Bavarian California Technology Center.

Disclosure: **M. Malania**, None; **J. Konrad**, None; **H. Jägle**, None; **J.S. Werner**, None; **M.W. Greenlee**, None

References

1. Ambati J, Ambati BK, Yoo SH, Ianchulev S, Adamis AP. Age-related macular degeneration: etiology, pathogenesis, and therapeutic strategies. *Surv Ophthalmol*. 2003;48:257–293.
2. Bressler NM, Bressler SB, Fine SL, et al. Age-related macular degeneration. *Surv Ophthalmol*. 1988;32:375–413.
3. Chakravarthy U, Augood C, Bentham GC, et al. Cigarette smoking and age-related macular degeneration in the EUREYE Study. *Ophthalmology*. 2007;114:1157–1163.
4. Francis PJ. Genetics of inherited retinal disease. *J R Soc Med*. 2006;99:189–191.
5. van Leeuwen R, Klaver CCW, Vingerling JR, Hofman A, de Jong PT. Epidemiology of age-related maculopathy: a review. *Eur J Epidemiol*. 2003;18:845–854.
6. Genead MA, Fishman GA, Stone EM, Allikmets R. The natural history of Stargardt disease with specific sequence mutation in the ABCA4 gene. *Invest Ophthalmol Vis Sci*. 2009;50: 5867–5871.
7. Walia S, Fishman GA. Natural history of phenotypic changes in Stargardt macular dystrophy. *Ophthalmic Genet*. 2009;30: 63–68.
8. Piermarocchi S, Varano M, Parravano M, et al. Quality of vision index: a new method to appraise visual function changes in age-related macular degeneration. *Eur J Ophthalmol*. 2011; 21:55–66.
9. Schuman SG, Koreishi AF, Farsiu S, Jung S, Izatt JA, Toth CA. Photoreceptor layer thinning over drusen in eyes with age-

related macular degeneration imaged in vivo with spectral-domain optical coherence tomography. *Ophthalmology*. 2009;116:488–496.

10. Mecklenburg L, Schraermeyer U. An overview on the toxic morphological changes in the retinal pigment epithelium after systemic compound administration. *Toxicol Pathol*. 2007;35:252–267.
11. Lund RD, Coffey PJ, Sauvé Y, Lawrence JM. Intraretinal transplantation to prevent photoreceptor degeneration. *Ophthalmic Res*. 1997;29:305–319.
12. Strettoi E, Porciatti V, Falsini B, Pignatelli V, Rossi C. Morphological and functional abnormalities in the inner retina of the rd/rd mouse. *J Neurosci*. 2002;22:5492–5504.
13. Rimayanti U, Kiuchi Y, Yamane K, et al. Inner retinal layer comparisons of eyes with exudative age-related macular degeneration and eyes with age-related macular degeneration and glaucoma. *Graefes Arch Clin Exp Ophthalmol*. 2014;252:563–570.
14. Lee EK, Yu HG. Ganglion cell–inner plexiform layer and peripapillary retinal nerve fiber layer thicknesses in age-related macular degeneration. *Invest Ophthalmol Vis Sci*. 2015;56:3976–3983.
15. Walia S, Fishman GA. Retinal nerve fiber layer analysis in RP patients using Fourier-domain OCT. *Invest Ophthalmol Vis Sci*. 2008;49:3525–3528.
16. Pasadhika S, Fishman GA, Allikmets R, Stone EM. Peripapillary retinal nerve fiber layer thinning in patients with autosomal recessive cone-rod dystrophy. *Am J Ophthalmol*. 2009;148:260–265.
17. Genead MA, Fishman GA, Anastasakis A. Spectral-domain OCT peripapillary retinal nerve fibre layer thickness measurements in patients with Stargardt disease. *Br J Ophthalmol*. 2011;95:689–693.
18. Ptito M, Schneider FCG, Paulson OB, Kupers R. Alterations of the visual pathways in congenital blindness. *Exp Brain Res*. 2008;187:41–49.
19. Noppeney U, Friston KJ, Ashburner J, Frackowiak R, Price CJ. Early visual deprivation induces structural plasticity in gray and white matter. *Curr Biol*. 2005;15:R488–R490.
20. Pan W-J, Wu G, Li C-X, Lin F, Sun J, Lei H. Progressive atrophy in the optic pathway and visual cortex of early blind Chinese adults: a voxel-based morphometry magnetic resonance imaging study. *Neuroimage*. 2007;37:212–220.
21. Mendola JD, Conner IP, Roy A, et al. Voxel-based analysis of MRI detects abnormal visual cortex in children and adults with amblyopia. *Hum Brain Mapp*. 2005;25:222–236.
22. Xiao JX, Xie S, Ye JT, et al. Detection of abnormal visual cortex in children with amblyopia by voxel-based morphometry. *Am J Ophthalmol*. 2007;143:489–493.
23. Lv B, He H, Li X, et al. Structural and functional deficits in human amblyopia. *Neurosci Lett*. 2008;437:5–9.
24. Yücel Y, Gupta N. Glaucoma of the brain: a disease model for the study of transsynaptic neural degeneration. *Prog Brain Res*. 2008;173:465–478.
25. Gupta N, Yücel YH. What changes can we expect in the brain of glaucoma patients? *Surv Ophthalmol*. 2007;52:(suppl 2):S122–S126.
26. Gupta N, Ang LC, Noël de Tilly L, Bidaisee L, Yücel YH. Human glaucoma and neural degeneration in intracranial optic nerve, lateral geniculate nucleus, and visual cortex. *Br J Ophthalmol*. 2006;90:674–678.
27. Kitajima M, Korogi Y, Hirai T, et al. MR changes in the calcarine area resulting from retinal degeneration. *AJNR Am J Neuroradiol*. 1997;18:1291–1295.
28. Boucard CC, Hernowo AT, Maguire RP, et al. Changes in cortical grey matter density associated with long-standing retinal visual field defects. *Brain*. 2009;132:1898–1906.
29. Plank T, Frolo J, Brandl-Rühle S, et al. Gray matter alterations in visual cortex of patients with loss of central vision due to hereditary retinal dystrophies. *Neuroimage*. 2011;56:1556–1565.
30. Hernowo AT, Boucard CC, Jansonius NM, Hooymans JMM, Cornelissen FW. Automated morphometry of the visual pathway in primary open-angle glaucoma. *Invest Ophthalmol Vis Sci*. 2011;52:2758–2766.
31. Hernowo AT, Prins D, Baseler HA, et al. Morphometric analyses of the visual pathways in macular degeneration. *Cortex*. 2014;56:99–110.
32. Ogawa S, Takemura H, Horiguchi H, et al. White matter consequences of retinal receptor and ganglion cell damage. *Invest Ophthalmol Vis Sci*. 2014;55:6976–6986.
33. Le Bihan D. Looking into the functional architecture of the brain with diffusion MRI. *Nat Rev Neurosci*. 2003;4:469–480.
34. Le Bihan D. Diffusion MRI: what water tells us about the brain. *EMBO Mol Med*. 2014;6:569–573.
35. Basser PJ, Mattiello J, LeBihan D. MR diffusion tensor spectroscopy and imaging. *Biophys J*. 1994;66:259–267.
36. Basser PJ, Pierpaoli C. Microstructural and physiological features of tissues elucidated by quantitative-diffusion-tensor MRI. *J Magn Reson B*. 1996;111:209–219.
37. Kim JH, Budde MD, Liang HF, et al. Detecting axon damage in spinal cord from a mouse model of multiple sclerosis. *Neurobiol Dis*. 2006;21:626–632.
38. Song SK, Sun SW, Ramsbottom MJ, Chang C, Russell J, Cross AH. Dysmyelination revealed through MRI as increased radial (but unchanged axial) diffusion of water. *Neuroimage*. 2002;17:1429–1436.
39. Song SK, Sun SW, Ju WK, Lin SJ, Cross AH, Neufeld AH. Diffusion tensor imaging detects and differentiates axon and myelin degeneration in mouse optic nerve after retinal ischemia. *Neuroimage*. 2003;20:1714–1722.
40. Beaulieu C. The basis of anisotropic water diffusion in the nervous system - a technical review. *NMR Biomed*. 2002;15:435–455.
41. Fox RJ, Cronin T, Lin J, et al. Measuring myelin repair and axonal loss with diffusion tensor imaging. *Am J Neuroradiol*. 2011;32:85–91.
42. Beer AL, Watanabe T. Specificity of auditory-guided visual perceptual learning suggests crossmodal plasticity in early visual cortex. *Exp brain Res*. 2009;198:353–361.
43. Desikan RS, Ségonne F, Fischl B, et al. An automated labeling system for subdividing the human cerebral cortex on MRI scans into gyral based regions of interest. *Neuroimage*. 2006;31:968–980.
44. Fischl B, van der Kouwe A, Destrieux C, et al. Automatically parcellating the human cerebral cortex. *Cereb Cortex*. 2004;14:11–22.
45. Rohde GK, Barnett AS, Basser PJ, Marenco S, Pierpaoli C. Comprehensive approach for correction of motion and distortion in diffusion-weighted MRI. *Magn Reson Med*. 2004;51:103–114.
46. Friston KJ, Ashburner J. Generative and recognition models for neuroanatomy. *Neuroimage*. 2004;23:21–24.
47. Sherbondy AJ, Dougherty RF, Ben-Shachar M, Napel S, Wandell BA. ConTrack: finding the most likely pathways between brain regions using diffusion tractography. *J Vis*. 2008;8(9):15.
48. Sherbondy AJ, Dougherty RF, Napel S, Wandell BA. Identifying the human optic radiation using diffusion imaging and fiber tractography. *J Vis*. 2008;8(10):12.
49. Hoffmann MB, Kaule FR, Levin N, et al. Plasticity and stability of the visual system in human achiasma. *Neuron*. 2012;75:393–401.
50. Raz N, Levin N. Cortical and white matter mapping in the visual system-more than meets the eye: on the importance of

functional imaging to understand visual system pathologies. *Front Integr Neurosci*. 2014;8:68.

51. Yeatman JD, Dougherty RF, Myall NJ, Wandell BA, Feldman HM. Tract profiles of white matter properties: automating fiber-tract quantification. *PLoS One*. 2012;7:e49790.
52. Fitzgibbon T, Taylor SF. Retinotopy of the human retinal nerve fibre layer and optic nerve head. *J Comp Neurol*. 1996;375: 238–251.
53. Jansonius NM, Nevalainen J, Selig B, et al. A mathematical description of nerve fiber bundle trajectories and their variability in the human retina. *Vision Res*. 2009;49:2157–2163.
54. Song S-K, Yoshino J, Le TQ, et al. Demyelination increases radial diffusivity in corpus callosum of mouse brain. *Neuroimage*. 2005;26:132–140.
55. Cheong JLY, Thompson DK, Wang HX, et al. Abnormal white matter signal on MR imaging is related to abnormal tissue microstructure. *AJNR Am J Neuroradiol*. 2009;30: 623–628.